A new sensor based on an amino-montmorillonite-modified inkjet-printed graphene electrode for the voltammetric determination of gentisic acid

A new sensor based on an amino-montmorillonite-modified inkjet-printed graphene electrode for the voltammetric determination of gentisic acid

Liliane M. Dongmo[1], Léopoldine S. Guenang[1,2], Sherman L. Z. Jiokeng[1,3], Arnaud T. Kamdem[4], Giscard Doungmo[1,5], Bassetto C. Victor[6], Milica Jović[6], Andreas Lesch[7], Ignas K. Tonlé[1], Hubert Girault[6]

Abstract

An amperometric sensor based on an inkjet-printed graphene electrode (IPGE) modified with amine-functionalized montmorillonite (Mt-NH_2) for the electroanalysis and quantification of gentisic acid (GA) has been developed. The organoclay used as IPGE modifier was prepared and characterized by infrared spectroscopy, X-ray diffraction, scanning electron microscopy, CHN elemental analysis, and thermogravimetry. The electrochemical features of the Mt-NH_2/IPGE sensor were investigated by cyclic voltammetry and electrochemical impedance spectroscopy. The sensor exhibited charge selectivity ability which was exploited for the electrochemical oxidation of GA. The GA amperometric response was high in acidic medium (Brinton-Robinson buffer, pH 2) due to favorable interactions between the protonated amine groups and the negatively charged GA. Kinetic studies were also performed by cyclic voltammetry, and the obtained electron transfer rate constant of 11.3 s^{-1} indicated a fast direct electron transfer rate of GA to the electrode. An approach using differential pulse voltammetry was then developed for the determination of GA (at + 0.233 V vs. a pseudo Ag/Ag^+ reference electrode), and under optimized conditions, the sensor showed high sensitivity, a wide working linear range from 1 to 21 μM ($R^2 = 0.999$), and a low detection limit of 0.33 μM (0.051 ± 0.01 mg L^{-1}). The proposed sensor was applied to quantify GA in a commercial red wine sample. The simple and rapid method developed using a cheap clay material could be employed for the determination of various phenolic acids.

Keywords Montmorillonite, Organoclay, Inkjet-printed graphene electrode, Electroanalysis, Gentisic acid

Introduction

Gentisic acid (GA) or 2,5-dihydroxybenzoic acid (Scheme 1) is a natural diphenolic compound deriving from benzoic acid, mostly found in several flowered plants and the root of the genus *Gentiana* [1, 2]. It is an aspirin metabolite excreted by the kidneys. There are many studies published on GA biological activities which highlighted its potential uses in the treatment of diseases. Also, epidemiological findings clearly established a good correlation between the consumption of rich diet phenolic acids such as GA and prevention of various diseases [3]. It has been used for the inhibition of low-density lipoprotein oxidation and protection against gamma radiation exposure and cyclophosphamide-induced

✉ Ignas K. Tonlé
itonle@yahoo.com

[1] Department of Chemistry, Electrochemistry and Chemistry of Materials, University of Dschang, Dschang, Cameroon

[2] Department of chemistry, Inorganic Chemistry Laboratory, University of Buea, Buea, Cameroon

[3] Laboratoire de Chimie Physique et Microbiologie pour les Matériaux et l'Environnement (LCPME), UMR 7564 CNRS – Université de Lorraine, 405, rue de Vandœuvre, 54600 Villers-lès-Nancy, France

[4] Institute of Microsystems Engineering IMTEK, Laboratory for Sensors, University of Freiburg, 79110 Freiburg, Germany

[5] Institute of Inorganic Chemistry, Christian-Albrechts-Universität zu Kiel, Max-Eyth-Straße 2, 24118 Kiel, Germany

[6] Laboratoire d'Electrochimie Physique et Analytique, EPFL, Rue de l'Industrie, CH-1951 Sion, Switzerland

[7] Department of Industrial Chemistry "Toso Montanari", University of Bologna, Viale del Risorgimento 4, 40136 Bologna, Italy

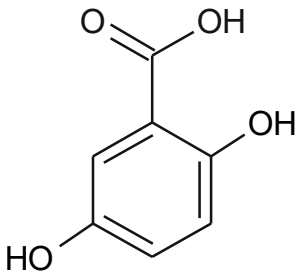

Scheme 1 Chemical structure of gentisic acid (GA)

genotoxicity. Farshad et al. recently provided a comprehensive review on pharmacological actions, pharmacokinetic properties, pharmaceutical applications, and also toxicity and adverse reactions of GA [4].

GA has affinity to connective tissue proteins, and higher retention of exogenous GA was demonstrated in humans with cancer [5]. GA acts against NRF2 (Nuclear factor erythroid-derived 2-like 2), an important transcription factor that regulates the synthesis of antioxidant molecules before its strong antioxidant effects as a free radical scavenger molecule [5]. GA is spread out in several drinks including red and white wines, and its presence above the standards (600 to 800 g kg^{-1} for a 70-kg person) can affect the health of human beings [6].

A number of analytical approaches such as high performance liquid chromatography [7–9], fluorescence detection [10], and capillary electrophoresis [11] have been suggested for the determination of GA. However, the high instrumentation and maintenance costs, the complexity in sample preparation, and the requirement of skilled operators constitute limitations to these techniques. At the opposite, electrochemical methods are renowned in analytical sciences since they are cost-effective, simple in manipulation, highly sensitive, and selective. Furthermore, composite electrodes can be miniaturized and designed for desired analytical tasks. To date, only one report is found in the literature for the electrochemical determination of GA, based on a polyphenol oxidase–modified carbon paste electrode that was proposed by Pedano and coworkers [12]. Thus, the development of inexpensive and rapid electroanalytical devices remains currently useful in the quantification of this compound.

For the elaboration of disposable, low-cost, and flexible electrochemical sensors, inkjet printing is nowadays an emerging technology. Yet, this technique can allow the preparation of miniaturized and mass-produced sensors for various analytical applications [13–16]. For example, inkjet-printed carbon nanotube electrodes were employed for measuring pyocyanin and uric acid in a wound fluid simulant and culture media [17]. Dalibor et al. exploited an inkjet-printed carbon nanotube electrode modified with dandelion-like MnO_2 microspheres for the determination of L-dopa, a dopamine precursor [18], and proposed a disposable biosensor based on amidase/CeO_2/GNR-modified inkjet-printed CNT electrodes for paracetamol detection in biological fluids [19]. More recently, Milos et al. reported the fabrication and application of a sensitive disposable inkjet-printed carbon nanotube electrodes modified with dimercaptosuccinic acid-capped Fe_3O_4 nanoparticles on reduced graphene oxide nanosheets, for the detection of trifluoperazine in biological fluids [20]. On the other hand, clay minerals and especially those chemically modified by organic molecules bearing functional groups (known as organoclays) have been proven to be prominent electrode modifiers [21]. Such materials have gained growing interest in the field of electrochemistry where they are exploited as electrode materials. They combine in a single structure the inherent properties of the starting clay (mechanical stability, well-known composition, large surface area, microporosity) and the chelating ability or ion exchange properties of the attached organic molecule. Furthermore, organoclay-based composite electrodes are increasingly exploited in preconcentration electroanalysis for the detection of either heavy metals [22–25] or organic molecules [26–29]. Therefore, we were interested in preparing a novel sensitive and disposable electrochemical sensor for GA detection, based on an inkjet-printed graphene electrode (IPGE) modified by an organoclay. The smectite-type clay mineral used in this work as electrode modifier was functionalized by the grafting of [3(2-aminoethyl)]propyltrimethoxysilane (AEP-TMS) and then characterized by infrared spectroscopy, X-ray diffraction, and scanning electron microscopy before application as electrode modifier. Key parameters involved in the electroanalytical detection of GA were optimized, and the effects of interfering compounds were investigated.

Experimental

Clay mineral, materials, and chemicals

The Na-montmorillonite (SWy-2, hereafter referred to as Mt-Na) clay mineral used in this work was acquired from the Source Clays Repository, University of Missouri-Columbia (Columbia, MO 65211, USA). Its chemical formula is $NaSi_{16}(Al_6FeMg)O_{20}(OH)_4$, and it possesses a cationic exchange capacity of about 0.764 meq g^{-1} [30]. All chemicals were obtained commercially and used without further purifications. Gentisic acid (GA, $C_7H_6O_4$, 99%) and hexaammineruthenium (III) chloride ($Ru(NH_3)_6Cl_3$, 98%) were purchased from Sigma-Aldrich (https://www.sigmaaldrich.com); H_3BO_3 (98%) and KCl (99.5%) were obtained from Fisher Scientific International (https://www.fishersci.com); CH_3COOH, H_3PO_4 (63%), K_2HPO_4 (99%), KH_2PO_4 (99%), and potassium hexacyanoferrate (III) ($K_3Fe(CN)_6$, Fluka) were purchased from Servilab (https://www.servilab.fr). Britton-Robinson buffer solutions were prepared from CH_3COOH, H_3BO_3, and H_3PO_4 at pH values

ranging from 2 to 5. The grafting agent ([3-(2-aminoethylamino)propyl] trimethoxysilane, AEP-TMS, ≥ 80%) used for clay modification was obtained from Sigma-Aldrich (https://www.sigmaaldrich.com). All solutions were prepared with purified water, and experiments were carried out at room temperature.

Grafting of AEP-TMS on the surface of montmorillonite

Amino-functionalized montmorillonite was prepared following a previously published procedure [31]. Briefly, 1 g of montmorillonite was dispersed in 50 mL of 0.1 M AEP-TMS in dry toluene. Afterwards, the resulting mixture was heated at 105 °C and allowed to reflux under stirring for 72 h in an inert N_2 atmosphere. The solid obtained was washed successively with toluene and ethyl alcohol and then filtered. The product Mt-NH_2 was finally dried for 2 h at 120 °C in an inert nitrogen atmosphere and stored in a flask.

Preparation of working electrodes

For the fabrication of inkjet-printed graphene electrodes (IPGEs), two platforms were subsequently used: the DMP-2850 inkjet printer from Fujifilm Dimatix was employed to deposit four inkjet-printed layers of the graphene dispersion (graphene ink for inkjet printing with ethyl cellulose in cyclohexanone and terpineol, Sigma-Aldrich), and then the X-Serie CeraPrinter from Ceradrop was used to simultaneously print and photopolymerize with an integrated UV LED (FireEdge FE300 380–420 nm; Phoseon Technology) a UV curable ink (EMD 6200 from Sun Chemical) as insulating material to define accurately the electrode area and to insulate partially the graphene patterns used as electronic traces. All printing parameters, such as the voltage pulse for the piezoelectric actuation inside the nozzles, jetting frequency, droplet falling speed, the overlapping distance of adjacent droplets, and substrate temperature, were optimized for each printed layer. After printing of the graphene ink, the patterns were thermally cured for 1 h in a furnace at 400 °C. The insulation layer was deposited as a frame around the graphene pattern to create a squared working electrode area of theoretically 1 mm^2. Afterwards, the IPGEs were modified by drop-coating of clay materials: 5 mg of either Mt-Na or Mt-NH_2 was each introduced into 1 mL of distilled water and submitted to ultrasonication for 30 min. Then, 0.5 μL (30 μg of clay) of each clay dispersion was removed using a micropipette and deposited on each IPGE active surface by "drop coating" and then dried in an oven at 110 °C for 1 min prior to use. Throughout the text, the modified electrodes are referred to as Mt-Na/IPGE and Mt-NH_2/IPGE for the IPGE modified by raw Mt-Na and Mt-NH_2, respectively.

Electrochemical procedures and apparatus

Electrochemical measurements were performed with the Palmsens[3] potentiostat (Palmsens) operated with the PS Trace 4.2 electrochemical analysis software and using a standard three-electrode cell. The voltammograms were recorded under quiescent conditions immediately after the immersion of the working electrode in a conventional single compartment cell containing the "analyte + electrolyte" solution, a pseudo reference electrode (Ag/Ag^+) and a platinum wire auxiliary electrode. Differential pulse voltammetry (DPV) measurements were performed in a 25-mL electrochemical cell containing 0.04 M Britton-Robinson buffer solution (BRBS) at precise pH and appropriate concentrations of GA in the potential range from 0.0 to 0.6 V. The pH of the solutions was monitored using an Inolab pH meter, and all experiments were conducted at room temperature. Electrochemical impedance spectroscopy (EIS) was carried out in 1 mM $[Fe(CN)_6]^{3-/4-}$ (1:1) solution containing 0.1 M KCl over the frequency range of 0.1 Hz–10 kHz. The morphology of raw and modi- fied clay was analyzed by scanning electron microscopy (SEM) on a JEOL JCM-6000 spectrometer (acceleration volt- age of 15 kV). Fourier transform infrared spectroscopy (FTIR) was used to assess the presence of organic groups in the final materials using a Nicolet 8700 type spectrometer equipped with a specular reflectance accessory (Smart Collector). The crystallinity of raw and modified clay materials was determined by X-ray diffraction analysis using a STOE Stadi-p X-ray powder diffractometer (Stoe & Cie GmbH, Darmstadt, Germany), with Cu Kα1 radiation (40 kV, 30 mA, and λ_{Cu} = 1.54056 Å). CHN elemental analysis was performed using CHNS Analyzer Euro EA 3000. The thermal behavior of the clay mineral before and after its modification was investigated by thermogravimetric analysis on a STA 409C equipment (Netzsch Geratebau GmbH, Germany). Approximately 10 mg of each dried sample was heated from 25 to 1000 °C under a nitrogen atmosphere with a heating rate of 10 °C min^{-1}.

Results and discussion

Characterization of inkjet-printed graphene electrodes

The unmodified IPGEs were analyzed by Raman spectroscopy, scanning electron microscopy (SEM), and X-ray photoelectron spectroscopy (XPS), and Fig. SI 1 (Electronic Supporting Material) presents the results obtained. The Raman spectra of IPGE (Fig. SI 1(A)) exhibited several peaks characteristic of graphene (sp^2 peak), namely, G at 1600 cm^{-1}. Apart from this peak, there is the D peak at 1300 cm^{-1}, the D' peak at 1610 cm^{-1}, and the 2D peak at 2700 cm^{-1}. The

presence of D and D' shows that the commercial ink contains defects or disorder [32, 33]. The 2D band also called G' as G band is used to determine the number of graphene layer [32, 34] through the ratio I_G/I_{2D} with a value of 4 which confirms that 4 graphene layers are printed on the substrate. Fig. SI 1(B) represents the SEM images of a bare IPGE, which clearly shows the layered structure of graphene used to elaborate the inkjet-printed electrode. The XPS spectra (Fig. SI 1(C) and 1(D)) revealed the presence of two functional groups identified on the C1s spectrum. Also, the presence of five chemical elements has been identified: carbon (72.11%), oxygen (23.49%), silicium (2.83%), nitrogen (1.17%), and phosphorus (0.4%). The first two elements appearing with a high percentage rate are the principal constituents of graphene, while the last three elements are most likely due to the insulation ink used to create the square surface of the inkjet-printed electrode.

Physico-chemical characterization of composite materials

The structural, morphological, and thermal characterizations of the montmorillonite before and after its chemical modification was performed. The FTIR spectra of natural montmorillonite (Mt-Na) and modified montmorillonite (Mt-NH_2) are presented in Fig. 1A. The stretching vibration bands on the raw clay mineral (Fig. 1A, curve (a)) at 3404 and 3630 cm^{-1} correspond to the physisorbed ν(O–H) and Si–OH of the octahedral sites of the clay, respectively [35, 36]. The band observed at 1640 cm^{-1} is attributed to the O–H bending from the physisorbed water molecules in the interlamellar space of montmorillonite. Some remarkable bands were also observed at 520 and 1020 cm^{-1} corresponding to the Si–O stretching [37]. However, after grafting the AEP-TMS (Fig. 1A, curve (b)), new asymmetric stretching bands were observed at

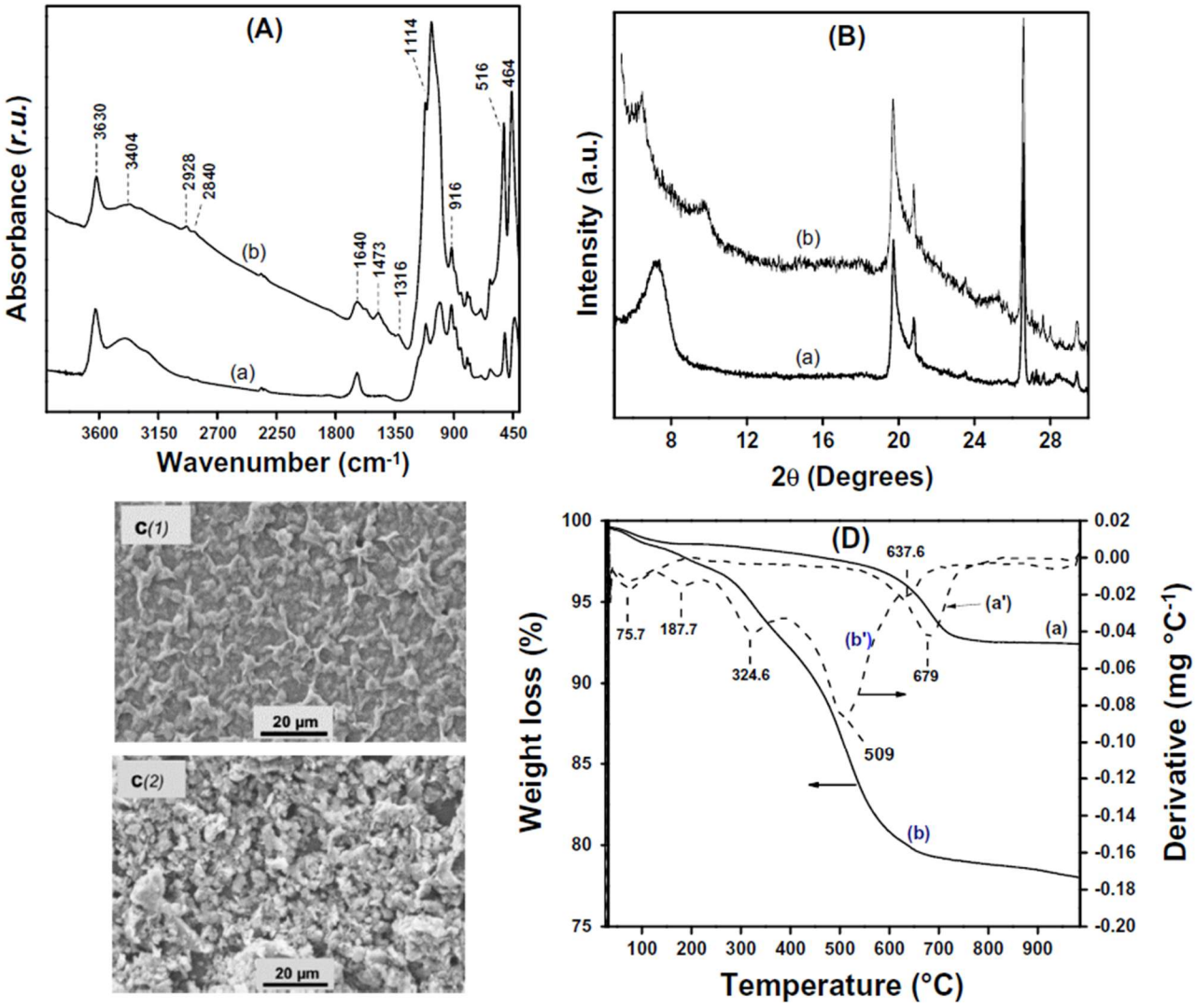

Fig. 1 (A) FTIR spectra, (B) X-ray diffraction patterns, (C) SEM micrographs, and (D) thermal analysis curves of Mt-Na (a, C(1)) and Mt-NH_2 (b, (C(2))

2928 cm^{-1} due to C–H bond [38], while the bands at 1454 and 1316 cm^{-1} were assigned to $-CH_2-$ scissoring, symmetric, and asymmetry, respectively, both from the silane coupling agent. XRD data were used to determine if the crystalline structure of the clay was altered after the organic modification processes. Figure 1B displays XRD patterns of the starting Mt-Na clay mineral and Mt-NH_2. The Mt-Na pattern of smectite clay (curve (a)) is characterized at low diffraction angles by a peak at $2\theta = 7.3°$ corresponding to a basal spacing of 12.1 nm [39–41]. A slight difference was observed after the grafting of AEP-TMS. The peak corresponding to the basal spacing d_{001} of the Mt-Na shifted to lower values of $2\theta = 6.5°$ (Fig. 1B, curve (b)) indicating an increase in the basal spacing from 1.21 to 1.36 nm. This result is attributed to grafting of AEP-TMS in the interlamellar space of the clay mineral, a common observation in organoclays issued from the intercalation or the grafting of guest species layered clay minerals [42, 43]. One can conclude that the organosilane molecules (AEP-TMS) were mainly hydrolyzed and condensed with the hydroxyl groups on the external surface of Mt.

The SEM images of raw Mt-Na and Mt-NH_2 are shown in Fig. 1C. On the image of Mt-Na (Picture C1), one can observe the strong tendency towards aggregation and the compact aspect of the material, with particles arranged in the form of agglomerates of irregular shape and flat surfaces. For Mt-NH_2 (Picture C2), the particles are even more agglomerated and present onto the electrode surface as bigger aggregates, suggesting that after functionalization, the organosilane moieties are aggregated on the surface of Mt-Na clay. The TG and DTG curves of the samples before and after grafting are shown in Fig. 1D. There are two major mass losses in the curves for Mt-Na sample (curves (a) and (a')). The first one (≈ 2%) occurred in the range of 30–300 °C and centered according to the DTG curve peak at ~ 75 °C. This mass loss is attributed to the removal of physisorbed water on the surface and interlayer space of montmorillonite. The second mass loss (≈ 5.6%) at ~ 679 °C is due to the dehydroxylation of octahedron layers in montmorillonite. For Mt-NH_2 sample, there are five mass losses (for a total of ≈ 21%) (Fig. 1D, curves (b) and (b')). The two mass losses around 76 °C and 188 °C are attributed respectively to the removal of physisorbed and zeolitic water, followed by the loss of hydration water and/or physically absorbed AEP-TMS at 325 °C. The fourth mass loss at 509 °C is due to the decomposition of grafted silane, concomitantly with the dehydroxylation of montmorillonite at 638 °C.

During the grafting reaction performed in dry solvent to avoid the polymerization of silane molecules, a condensation reaction between the silane and the −OH groups of the mineral backbone generally occurs that leads to a strong binding of the organic molecule to the inorganic surface [44–48]. Thus, elemental analysis was performed on the amino-grafted material (Mt-NH_2) for C, H, and N. The results obtained were 11.07% C, 2.60% H, and 4.66% N. This was an evidence of the presence of nitrogen-containing moieties on the grafted clay. To determine the structural formula of the organoclay, the coupling of AEP-TMS was assumed to occur on one structural unit of Mt (formula: $NaSi_{16}(Al_6FeMg)O_{20}(OH)_4$)) via one, two, three, or four methoxy groups. The theoretical content was C, 11.34%; H, 2.72%; and N, 3.78%. The mechanism proposed in Scheme 2 meets the experimental results that support the idea of the chemical bonding of AEP-TMS on Mt clay material as revealed by infrared results. Based on these theoretical and experimental data of CHN elemental analysis, the calculated structural formula of Mt-NH_2 was $NaSi_{16}(Al_6FeMg)O_{20}(OH)_2[OSi(OCH_3)_2(CH_2)_3NH(CH_2)_2NH_2]_2$.

Cyclic voltammetry characterization of electrodes

The electrochemical characterization of each sensor was first performed in solution with neutral pH using cyclic voltammetry (CV). Negatively charged ($[Fe(CN)_6]^{3-}$) and positively charged ($[Ru(NH_3)_6]^{3+}$) redox probes were used to verify and confirm the ionic exchange features of the prepared sensors. The analysis of $[Fe(CN)_6]^{3-}$ was carried out within a potential ranging from − 0.3 to 0.6 V in 0.1 M KCl, and the results are depicted in Fig. 2a and b. As shown, the response of the probe on IPGE (dotted line in Fig. 2a) was reversible and showed both oxidation and reduction peaks with the following currents: $I_{pa} = 0.807$ μA (anodic) and $I_{pc} = 0.843$ μA (cathodic). From the bare IPGE to Mt-Na/IPGE, these currents were significantly reduced ($I_{pa} = 0.114$ μA and $I_{pc} = 0.105$ μA) as also revealed by Fig. 2a. Moreover, Mt-Na/IPGE did not accumulate $[Fe(CN)_6]^{3-}$ upon continuous cycling since a steady state characterized by constant peak currents in both anodic and cathodic directions was rapidly reached. These

Scheme 2 Proposed mechanism for the grafting of AEP-TMS on Mt-Na

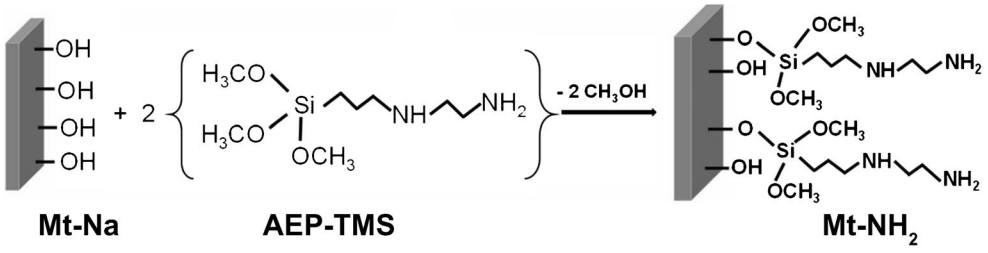

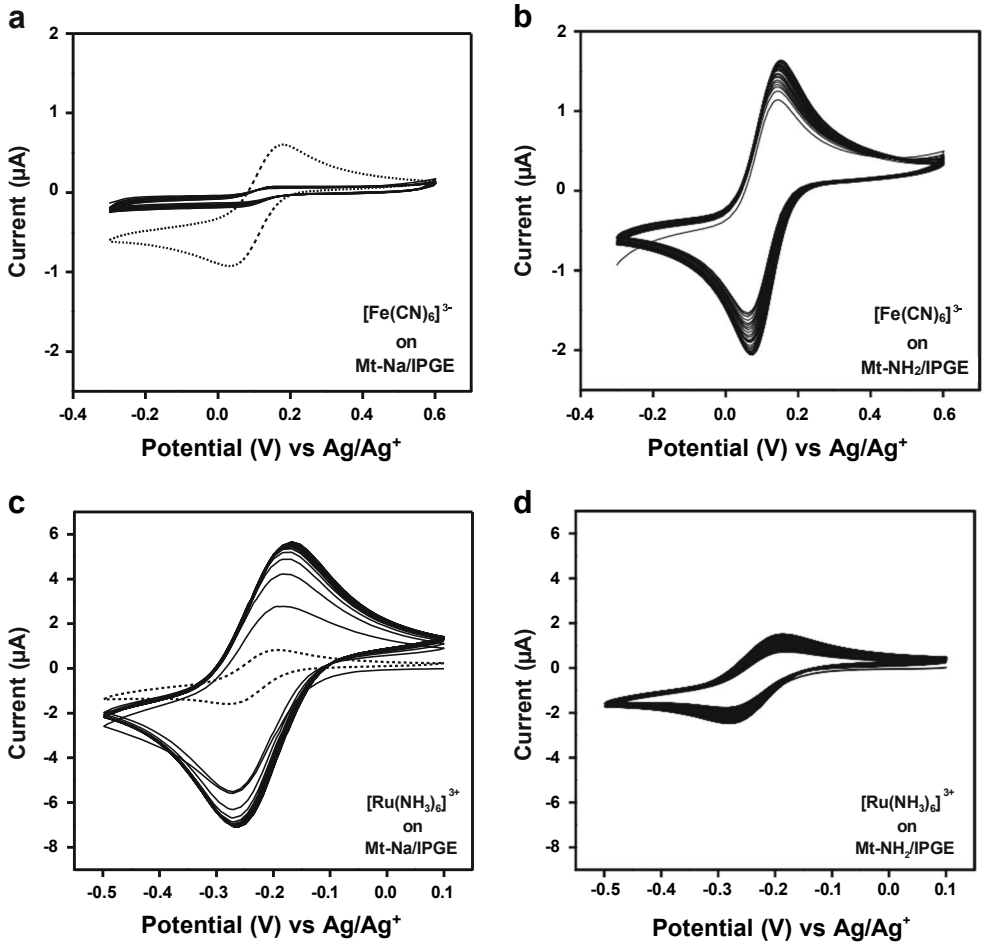

Fig. 2 Multisweep cyclic voltammograms recorded in 0.1 M KCl containing (a, b) 0.5 mM $[Fe(CN)_6]^{3-}$ and (c, d) 0.5 mM $[Ru(NH_3)_6]^{3+}$ on IPGE coated with Mt-Na (a, c) and Mt-NH_2 (b, d). The dot line in a and c corresponds to bare IPGE (v = 20 mV s^{-1})

observations could be reasonably explained by electrostatic repulsion between the negatively charged clay sheets on the IPGE and $[Fe(CN)_6]^{3-}$ ions, consistent with previously published data [23, 49]. Thereafter the Mt-Na/IPGE working electrode was replaced in the supporting electrolyte by Mt-NH_2/IPGE.

In contrast, highest peak currents (I_{pa} = 1.775 μA, I_{pc} = 1.868 μA) and a slight accumulation were obtained with Mt-NH_2/IPGE (Fig. 2b). This accumulation could be due to electrostatic attraction between the negatively charged redox system $[Fe(CN)_6]^{3-}$ and the positively charged amino groups ($-NH_3^+$) present on the organosilane moieties previously grafted at the clay surface. Similarly, the analysis of $[Ru(NH_3)_6]^{3+}$ ions was carried out in the potential range from − 0.5 to 0.1 V in 0.1 M KCl, and results are presented in Fig. 2c and d. The response of the probe on IPGE (Fig. 2c) was also reversible and showed both oxidation and reduction peaks with current values at 1.094 μA (anodic) and 1.136 μA (cathodic). The comparison of the signal in Fig. 2c and d revealed that the oxidation and reduction peaks are less intense on the bare IPGE and Mt-NH_2/IPGE (I_{pa} 2.110 μA, I_{pc} 2.164 μA) (Fig. 2d) compared to Mt-Na/IPGE (I_{pa} 5.490 μA, I_{pc} 6.187 μA) (Fig. 2c). It was also observed a poor accumulation of $[Ru(NH_3)_6]^{3+}$ ions on Mt-Na/IPGE. This behavior is consistent with the favorable attraction phenomenon between $[Ru(NH_3)_6]^{3+}$ ions and the negatively charged montmorillonite sheets. On the other hand, the lower peak current and non-accumulation obtained on Mt-NH_2/IPGE might be explained by the fact that the protonated organoclay film acted as an electrostatic barrier, preventing the uptake of the cationic $[Ru(NH_3)_6]^{3+}$ species. This demonstrates that the charge selectivity of the protonated amino clay material remained effective on IPGE surface, enabling fast transport/accumulation of anions while preventing the uptake of the positively charged species. This result is promising for the exploitation of Mt-NH_2/IPGE as an electrochemical sensor for GA. Before that, it seemed useful to further characterize the materials to be used as electrode modifiers, to get more informations regarding their ability to charge transfer by EIS spectroscopy.

Electrochemical impedance spectroscopy results

The ideal redox system $[Fe(CN)_6]^{3-/4-}$ was used to evaluate the electrochemical properties of different electrodes prepared herein. EIS measurements were performed in 5 mM of $K_3[Fe(CN)_6]/K_4[Fe(CN)_6]$ (1:1) solution containing 0.1 M

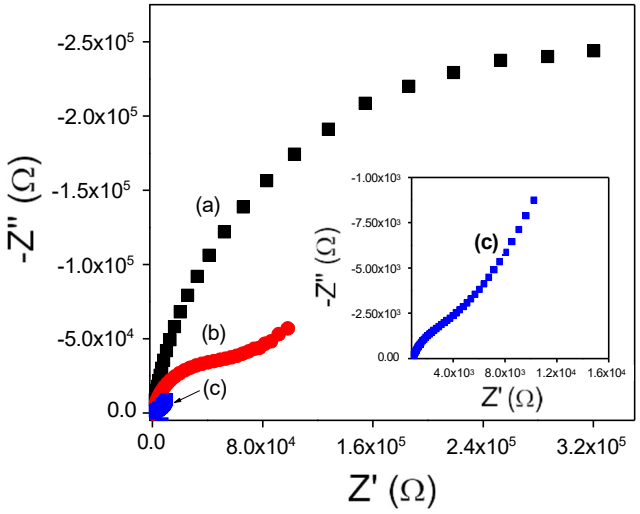

Fig. 3 EIS spectra in 0.1 M KCl containing 5 mM $[Fe(CN)_6]^{3-/4-}$ at various electrodes: (a) bare IPGE, (b) Mt-Na/IPGE, and (c) Mt-NH_2/IPGE. The inset corresponds to the Nyquist plot of Mt-NH_2/IPGE

KCl, over the frequency range 10^{-4}–10 kHz. The Nyquist plots of EIS for bare IPGE, Mt-Na/IPGE, and Mt-NH_2/IPGE are provided in Fig. 3, where the semicircle diameter represents the charge transfer resistance (R_{ct}) of the electrode. The unmodified IPGE displays a non-negligible R_{ct} value of 8.80 Ω. When using Mt-Na/IPGE, the largest semicircle was obtained, with the highest charge transfer resistance of 14.29 Ω explained by some shielding behavior of the negatively charged Mt-Na clay particles on the anionic $[Fe(CN)_6]^{3-/4-}$ species as previously demonstrated by cyclic voltammetry studied. Finally, the Mt-NH_2/IPGE sensor exhibited the smallest semicircle (R_{ct} = 1.96 Ω), indicating its excellent electrical conductivity and the fact that the aminated clay promotes the transport properties of $[Fe(CN)_6]^{3-/4-}$ species.

Electrochemical behavior of GA at Mt-NH_2/IPGE and effect of scan rate

The electrochemical behavior of 0.2 mM GA was examined in 0.04 M BRBS (pH 2) on different electrodes using cyclic voltammetry, and the corresponding voltammograms are depicted in Fig. 4a. On these electrodes, a peak was obtained around 0.3 V in the anodic direction; by reversing the potential scan, a reduction peak was observed at 0.25 V. The optimum response based on sensitivity was recorded on Mt-NH_2/IPGE sensor in comparison with the bare IPGE and the same electrode covered by a thin film of Mt-Na clay mineral. The biggest response of GA on Mt-NH_2/IPGE in comparison with Mt-Na/IPGE could result in one hand from the intrinsic adsorptive ability of the clay mineral (as a pointed by the surface area of montmorillonite) deposited as thin film on the IPGE, and in another hand from favorable interaction between the protonated amine groups and the negatively charged GA. It is also reasonable to evoke the presence O and N atoms on Mt-NH_2 that can favor the formation of hydrogen bonding interactions with hydroxyl groups of GA.

DPV was used for quantification with information on the sensibility of the Mt-NH_2/IPGE sensor towards the detection of GA as shown in Fig. 4b. The DPV peak currents recorded in 0.04 M BRBS (pH 2) on the bare IPGE, Mt-Na/IPGE, and

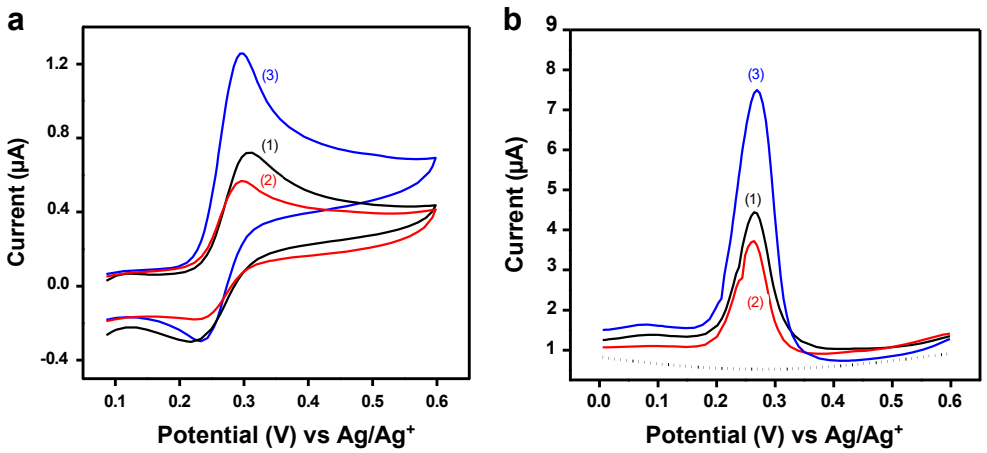

Fig. 4 a Cyclic voltammograms with scan rate 50 mV s^{-1} and b differential pulse voltammograms recorded for 0.2 mM GA in 0.04 M BRBS (pH 2) at the IPGE (1), Mt-Na/IPGE (2), and Mt-NH_2/IPGE (3). The dotted line in b is the curve recorded in the blank electrolyte on Mt-NH_2/IPGE

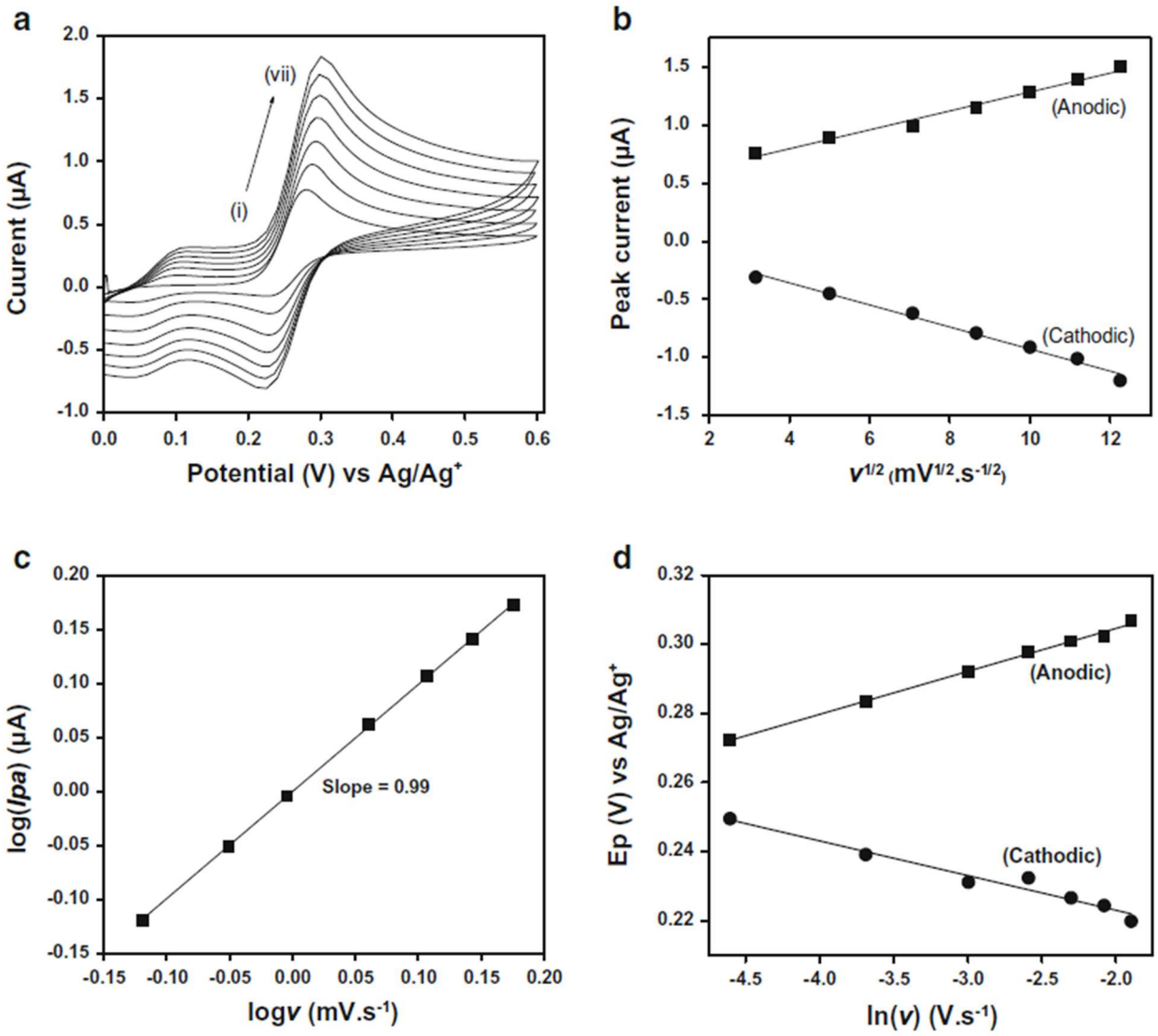

Fig. 5 a Cyclic voltammograms recorded in 0.04 M BRBS (pH 2) containing 0.2 mM GA on Mt-NH_2/IPGE at different scan rates (10, 25, 50, 75, 100, 125, and 150 mV s^{-1}), b peak current as a function of $v^{1/2}$, c log(*Ipa*) as a function of log(*v*), and d E_p (anodic and cathodic) as a function of ln*v*

Mt-NH_2/IPGE were 3.20, 2.73, and 6.10 μA, respectively. These results showed that the GA response on Mt-NH_2/IPGE is significantly improved due to the presence of the organoclay on the IPGE. This indicates an ability of Mt-NH_2 to induce effective enhancement of GA oxidation signal and improved electron transfer rates, confirming the existence of

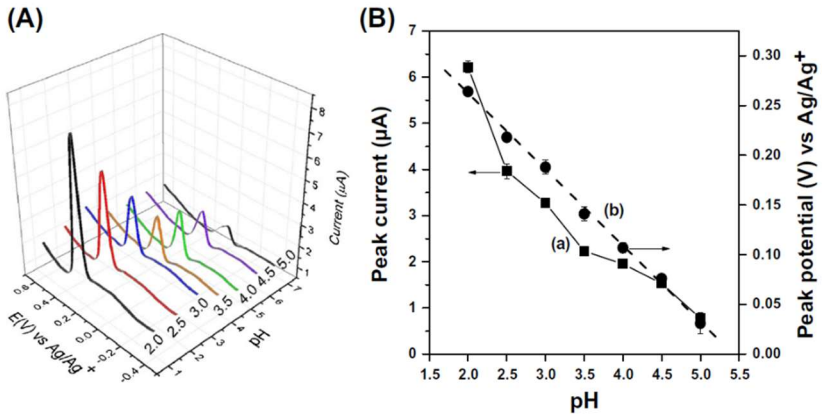

Fig. 6 (A) Effect of pH of the supporting electrolyte on the electrochemical response of 0.2 mM GA in 0.04 M BRBS on a Mt-NH_2/IPGE and (B) I_{pa} as a function of pH (a) and linear relationship between E_p and pH (b)

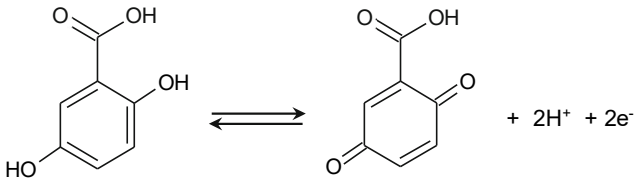

Gentisic acid **Benzoquinone-carboxylic acid**

Scheme 3 Electrochemical reaction process of GA acid at Mt-NH_2/IPGE

both accumulation and electrocatalytic effects as suggested above, originating from the organoclay materials with respect to the detection of GA. Therefore, our investigations were further focused on Mt-NH_2/IPGE as a working electrode.

Cyclic voltammetry was used to study the effect of potential scan rate (v) on the peak currents (I_p) and peak potentials (E_p) of GA, to gain more information about the kinetics of the electrochemical reaction of GA at Mt-NH_2/IPGE. Thus, by varying v between 10 and 150 mV s^{-1}, the voltammograms of 0.2 mM GA in 0.04 M BRBS (pH) were recorded, and as shown in Fig. 5a,a couple of quasi-reversible redox peaks of GA was obtained on each voltammogram at different scan rates. Upon this variation, the redox peak currents were dependent on the potential scan rate and gradually increased with this parameter. Also, these peak currents show linear dependence with the square root of the potential scan rate ($v^{1/2}$) (Fig. 5b). This indicates an adsorption-controlled process, a fact that was also confirmed by plotting the double logarithmic of I_{pa} vs. scan rate (Fig. 5c) with a slope ($\partial \log(I_{pa})/\partial \log(v)$) equal to 1 which is the characteristic value of an adsorption-controlled electron transfer mechanism [50]. With the increase of scan rate, the oxidation peak potentials (E_{pa}) moved to the positive direction, while the reduction peak potentials (E_{pc}) shifted to the negative direction, concomitantly with an increase of the ΔE_p value, indicating a quasi-reversible process. The relationship between peak potential (E_p) and ln v was summarized by two linear regression equations: E_{pa} (V) = 0.012 ln$v$ (V s^{-1}) + 0.330 (R = 0.998), and E_{pc} (V) = − 0.010 ln$v$ (V s^{-1}) + 0.205 (R = − 0.982). Some kinetic parameters were calculated following Laviron's equation [51]:

$$Epa = E^{o'} + m\left[0.78 + \ln\left(D^{1/2}k_s^{-1}\right) - 0.5\ln nm\right] + m/2\ln v, \quad m = RT/(1-\alpha)nF \tag{1}$$

$$Epc = E^{o'} - m'\left[0.78 + \ln\left(D^{1/2}k_s^{-1}\right) - 0.5\ln nm'\right] - m'/2\ln v, \quad m' = RT/\alpha nF \tag{2}$$

$$\log k_s = \alpha\log(1-\alpha) + (1-\alpha)\log\alpha - \log(RT/nFv) - [(1-\alpha)\alpha F/2.3RT]\Delta Ep \tag{3}$$

A value of 2.31 ≈ 2 for n could be obtained as the number of electrons transferred in the redox process of GA, and a charge transfer coefficient (α) was calculated to be 0.55 through the slopes of Eqs. (1) and (2). From the slope values of ΔE_p versus the logarithm of scan rate, the electron transfer rate constant (k_s) was calculated using Eq. (3), and a value of 11.3 s^{-1} was obtained. This k_s value of Mt-NH_2/IPGE was relatively high, which indicates a fast direct electron transfer rate of GA to the electrode surface.

Influence of pH on the peak potential and current of GA

Before using the proposed sensor for the quantification of GA, some parameters were optimized. The effect of the pH of the supporting electrolyte on GA oxidation was first evaluated at Mt-NH_2/IPGE by using DPV technique. The BR buffer pH

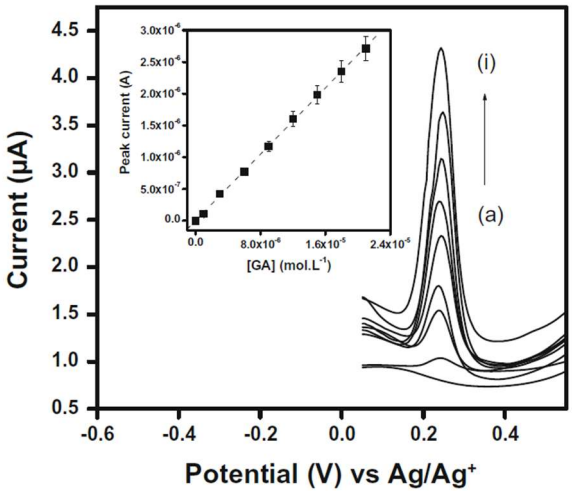

Fig. 7 DPV curves obtained under optimized conditions in 0.04 M BRB solution (pH 2) at different concentrations of GA: 0, 1, 3, 6, 9, 12, 15, 18, and 21 μM (a–i). The inset shows the corresponding calibration graph

Table 1 An overview on common analytical methods for the determination of GA

Detection method	Linear range (mg L^{-1})	LOD (mg L^{-1})	Detection medium	Reference
CZE-LIF	/	0.08	Urine	[11]
HPLC-FLD	0.05–2.5	0.015	Wine	[49]
HPLC with UV detection	2–40	0.001	Blood and plasma	[52]
HPLC with UV detection	0.0005–0.1	0.0025	Rabbit plasma and urine	[53]
GC/MS	0.23–1.86	0.024	Wine	[56]
HPLC connected ESI-MS	9×10^{-6}–58.2×10^{-6}	5.06×10^{-6}	Human plasma	[57]
LC–MS/MS	0.33×10^{-6}–24×10^{-4}	0.33×10^{-6}	Cell lysate	[58]
DPV	0.154–3.24	0.051	BRB	This work
	0–1.85	0.42	Wine	–

CZE-LIF capillary zone electrophoresis-laser-induced fluorescence, *ESI-MS* electrospray ionization mass spectrometry, *HPLC-FLD* high performance liquid chromatography with fluorescence detection, *DPV* differential pulse voltammetry, *LC–MS/MS* liquid chromatography-tandem mass spectrometry, *BRB* Britton-Robinson buffer

was thus varied in acidic medium, from 2.0 to 5.0 (Fig. 6A). The electrode response was highest in the most acidic medium (pH 2) and then started to decrease with an increase in pH (Fig. 6B, curve (a)). Around pH 5, the peak current becomes very weak. The results also showed that the oxidation peak potential of GA on Mt-NH_2/IPGE shifted to more negative values with rising the solution pH, an indication that protons are involved in the reaction process at the electrode surface. Besides, the anodic peak potential (E_{pa}) followed a linear dependence over pH (Fig. 6B, curve b), with a slope of 0.076 V/pH ($R^2 = 0.9995$). This signifies that an equal number of electrons and protons are involved in the redox mechanism of GA, according to the Nernst equation. From the above results, it appeared that two electrons and two protons are involved in the oxidation of GA to benzoquinone carboxylic acid (3,6-dioxocyclohexa-1,4-diene-1-carboxylic acid), and a reasonable reaction mechanism of GA at Mt-NH_2/IPGE was proposed in Scheme 3. To conclude this section, a BR buffer solution at pH 2 was chosen as a basic electrolyte for further experiments.

Calibration plot

Subsequently to the evaluation of pH effect, some DPV parameters were optimized, such as pulse amplitude (tested range 10–100 mV), potential step (2–20 mV), and equilibrium time (4–16 s). Each of these parameters was varied by keeping the other constant, and the obtained optimum values were the following: pulse amplitude 50 mV, potential step 5 mV, and equilibrium time 5 s. Under optimal conditions, the calibration plot was performed upon consecutive addition of GA from a standard solution into the supporting electrolyte (0.04 M BRBS at pH 2). The DPV peak currents recorded in these conditions (each concentration in four replicates) are provided in Fig. 7: the peak current (I_{pa}) increased with the increase of GA concentration in the investigated working range (1 to 21 μM). As shown by the inset in Fig. 7, the plot of the current of the oxidation peak versus the concentration of GA showed a linear dependence in the investigated range, with the regression equation of I_{pa} (μA) = 0.1303 C (M) + 4.423×10^{-9} ($R^2 = 0.9997$). The limit of detection of GA was found to be 0.33 μM (0.051 mg L^{-1}), defined by the relation $3S_b/m$ [52] (where S_b represents the standard deviation obtained from the blank and m the slope on the calibration plot). This demonstrates that Mt-NH_2/IPGE sensor can be used for the electroanalysis of GA in aqueous medium down to μM range, or in various other matrices. Yet, the contents of GA in red wines produced from different grape varieties are usually between 0.93 and 9.93 mg L^{-1} [53]. Also, GA concentration in healthy leaves of greening-tolerant and susceptible citrus species and

Table 2 Effect of some interfering organic species on the signal of 12 μM GA

Interfering compounds	Concentration of added species (μM)	Increase (%) in peak current of GA
Ascorbic acid	12	6.69 ± 0.32
Citric acid	12	9.02 ± 1.58
Dopamine	12	6.87 ± 0.50
Aspirin	12	19.40 ± 4.83
Gallic acid	12	14.30 ± 2.41
D(+)-glucose	12	7.70 ± 1.30

Experiments were performed in triplicate

cultivars is between 32.56 and 300 μg g^{-1} [54], while the free GA contents (in mg kg^{-1}) in some fruits are the following: gooseberry (2.01 ± 0.40), strawberry (30.85 ± 2.10), and orange (0.20 ± 0.12) [55].

The relative standard deviation (RSD) for five measurements with the same Mt-NH_2/IPGE was 3.7%. Also, three Mt-NH_2/IPGEs were prepared under the same conditions and showed an affordable reproducibility with RSD of 3.3%. Lastly, the peak currents slightly decreased to 90.7% from their initial values after the electrode was stored at room temperature for 2 weeks. The method proposed herein was compared with some data already reported in the literature on the detection and quantification of GA, as shown in Table 1. Overall, the obtained results indicated a good stabil- ity, repeatability, and sensitivity of Mt-NH_2/IPGE sensor, which can be exploited as promising analytical tool for the determination of GA.

Interference study and analytical application

The interference of some potential interfering organic species was investigated to evaluate the selectivity of the proposed sensor. The effect of the presence of citric acid, dopamine, ascorbic acid, gallic acid, aspirin, and D(+)-glucose usually present in biological matrices was hence studied towards GA DPV signal. The optimal conditions were applied to analyze a solution containing GA and each interference substance, both introduced in supporting the same concentration. The results obtained are given in Table 2. For all abovementioned compounds, it was found an increase in the amperometric signal of GA. However, apart from aspirin and gallic acid which increased the peak current of the target analyte to more than 10%, other investigated compounds did not significantly interfere. This interference effect could be probably due to fierce competition between these compounds and GA by accumulation sites of the grafted clay material. These results suggest that the procedure established herein could be considered selective for the quantification and detection of GA.

The ability of the modified electrode for the determination of GA in a real sample was demonstrated by applying the Mt-NH_2/IPGE sensor to analyze a commercial red wine (Merlot grape variety, from Bordeaux (France) and produced in 2019) following the standard addition method. The wine sample was used without any purification, extraction, or distillation. Figure SI 2 (Electronic Supporting Material) shows the DPV curves recorded in the red wine sample, while the inset gives the relation between peak current and GA concentration. From Fig. SI 2, GA was clearly detected in Merlot red wine as revealed by the first voltammogram. Using the calibration curve $I_{pa}(A) = 0.0788 \times C(M) + 2.13 \times 10^{-7}$, the concentration of GA was found to be 2.70 μM, which correspond to (0.42 ± 0.02) mg L^{-1} of GA. This value is slightly higher than data previously obtained on wines from the same grape variety (GA concentration between 0.20 and 0.31 mg L^{-1}) and of the same quality, although vintage years are different [53]. Other phenolic compounds and acids (ascorbic acid, gallic acid, salicylic acid) were listed as the same red wine contents. The affinity of amino groups on the organoclay with these biomolecules could explain such a result, which somehow limits the selectivity of the Mt-NH_2/IPGE sensor.

Conclusion

In this work, a sensitive amperometric sensor based on the successful immobilization of an aminated montmorillonite clay mineral (Mt-NH_2) on an inkjet-printed graphene electrode (IPGE) was proposed for the detection of GA. Under optimal conditions, the modified material proved to be a good electrode modifier for the electrochemical detection by differential pulse voltammetry of GA. The developed sensor has the advantages of a wide linear range, a low detection limit, and good repeatability for the detection of GA. It should be noted that one of the drawbacks is the low selectivity towards biomolecules, which makes it difficult to detect and quantify GA in different wines where the metabolites of GA can be found at high concentrations. Nonetheless, the Mt-NH_2/IPGE sensor has displayed interesting analytical performances, good stability and reproducibility, and an excellent detection limit and constitutes a prominent analytical tool for the determination of GA.

Acknowledgments L. S. Guenang thanks the Agence Universitaire de la Francophonie (France) for a travel grant.

Funding This work was supported by the Alexander von Humboldt Foundation (Germany).

Compliance with ethical standards

Conflict of interest The authors declare that they have no competing interests.

References

1. Levy G, Tsuchiya T (1972) Salicylate accumulation kinetics in man. New Engl J Med 287:430–432. https://doi.org/10.1056/NEJM197208312870903
2. Cavalcante FML, Almeida IV, Dusman E, Mantovani MS, Vicentini VEP (2018) Cytotoxicity, mutagenicity, and antimutagenicity of the gentisic acid on HTC cells. Drug Chem Toxicol 41(2):155–161. https://doi.org/10.1080/01480545.2017.1322606

3. Ashidate K, Kawamura M, Mimura D, Tohda H, Miyazaki S, Teramoto T, Yamamoto Y, Hirata Y (2005) Gentisic acid, an aspirin metabolite, inhibits oxidation of low-density lipoprotein and the formation of cholesterol ester hydroperoxides in human plasma. Eur J Pharmacol 513(3):173–179. https://doi.org/10.1016/j.ejphar.2005.03.012
4. Farshad A, Bibi MR, Hossein H (2020) A review on gentisic acid as a plant derived phenolic acid and metabolite of aspirin: comprehensive pharmacology, toxicology, and some pharmaceutical aspects (2020). Phytother Res 34(4):729–741. https://doi.org/10.1002/ptr.6573
5. Rosenberg EF, Krevsky DA, Kagan BM (1952) Laboratory and clinical experience with sodium gentisate in rheumatic disease. Ann Intern Med 36(6):1513–1519. https://doi.org/10.7326/0003-4819-36-6-1513
6. Altinoz MA, Elmaci I, Ozpinar A (2018) Gentisic acid, a quinonoid aspirin metabolite in cancer prevention and treatment - new horizons in management of brain tumors and systemic cancers. J Cancer Res Oncobiol 1(2):109–127. https://doi.org/10.31021/jcro.20181109
7. Ting AY, Kaushalya SD, Barry L, Zayed H, Sanjeewa G (2018) Development and validation of high performance liquid chromatographic method for determination of gentisic acid and related renal cell carcinoma biomarkers in urine. Microchem J 137:85–89. https://doi.org/10.1016/j.microc.2017.09.024
8. Kaushalya SD, Sanjeewa G, Undugodage DNP, Barry KL (2020) Analysis of gentisic acid and related renal cell carcinoma biomarkers using reversed-phase liquid chromatography with water-rich mobile phases. J Liq Chromatogr Relat Technol 42:681–687. https://doi.org/10.1080/10826076.2019.1666275
9. Chen S, Burton C, Kaczmarek A, Shi H, Ma Y (2015) Simultaneous determination of urinary quinolinate, gentisate, 4-Hydroxybenzoate, and a-ketoglutarate by high-performance liquid chromatography-tandem mass spectrometry. Anal Methods 7: 6572–6578. https://doi.org/10.1039/C5AY01643F
10. Jose A, Murillo P, Aurelia AM (1994) Matrix isopotential synchronous fluorescence direct determination of gentisic acid in urine. Anal Chim Acta 296:87–97. https://doi.org/10.1016/0003-2670(94)85153-0
11. Sandra Z, Xin Z, Jonathan S, Wolfgang T (2001) Determination of salicylate, gentisic acid and salicyluric acid in human urine by capillary electrophoresis with laser-induced fluorescence detection. J Chromatogr B 752:17–31. https://doi.org/10.1016/S0378-4347(00)00507-7
12. Pedano ML, Rivas GA (2000) Amperometric biosensor for the quantification of gentisic acid using polyphenol oxidase modified carbon paste electrode. Talanta 53:489–495. https://doi.org/10.1016/S0039-9140(00)00515-4
13. Lesch A, Salazar FC, Bassetto VC, Amstutz V, Girault HH (2015) Inkjet printing meets electrochemical energy conversion. Chimia 69:284–289. https://doi.org/10.2533/chimia.2015.284
14. Moya A, Gabriel G, Villa R, del Campo FJ (2017) Inkjet-printed electrochemical sensors. Sens Biosens 3:29–39. https://doi.org/10.1016/j.coelec.2017.05.003
15. Dong S, Wang Z, Asif M, Wang H, Yu Y, Hu Y, Liu H, Xiao F (2017) Inkjet printing synthesis of sandwiched structured ionic liquid-carbon nanotube-graphene film: toward disposable electrode for sensitive heavy metal detection in environmental water samples. Ind Eng Chem Res 56:1696–1703. https://doi.org/10.1021/acs.iecr.6b04251
16. Lesch A, Salazar FC, Prudent M, Delobel J, Rastgar S, Lion N, Tissot JD, Tacchini P, Girault HH (2014) Large scale inkjet-printing of carbon nanotubes electrodes for antioxidant assays in blood bags. J Electroanal Chem 717-718:61–68. https://doi.org/10.1016/j.jelechem.2013.12.027
17. Romana J, Sandra EM, Margaret G, Milica J, Hubert HG, Andreas L, Michael M, Christopher W, Greg MS (2019) Inkjet-printed carbon nanotube electrodes for measuring pyocyanin and uric acid in a wound fluid simulant and culture media. Anal Chem 91:8835–8844. https://doi.org/10.1021/acs.analchem.8b05591
18. Dalibor MS, Milica J, Milos O, Andreas L, Martin F, Hubert HG, Bratislav A (2019) Point-of-care amperometric determination of L-dopa using an inkjet-printed carbon nanotube electrode modified with dandelion-like MnO_2 microspheres. Microchim Acta 186: 532–539. https://doi.org/10.1007/s00604-019-3644-x
19. Dalibor MS, Milos O, Milica J, Valentina C, Andreas L, Hubert HG, Marija GJ, Bratislav A (2019) Disposable biosensor based on amidase/CeO_2/GNR modified inkjet-printed CNT electrodes-droplet based paracetamol detection in biological fluids for "point-of-care" applications. Electroanalysis 31:1–10. https://doi.org/10.1002/elan.201900129
20. Milos O, Dalibor MS, Milica J, Milena K, Andreas L, Hubert HG, Bratislav VA (2020) Inkjet-printed carbon nanotube electrodes modified with dimercaptosuccinic acid-capped Fe3O4 nanoparticles on reduced graphene oxide nanosheets for single-drop determination of trifluoperazine. ACS Appl Nano Mater. https://doi.org/10.1021/acsanm.0c00661
21. Tonle IK, Ngameni E, Tchieno FMM, Walcarius A (2015) Organoclay-modified electrodes: preparation, characterization and recent electroanalytical applications. J Solid State Electrochem 19: 1949–1973. https://doi.org/10.1007/s10008-014-2728-0
22. Ymele E, Jiokeng ZSL, Bup-Nde D, Kamgaing T, Tonle IK (2019) Simultaneous voltammetric determination of Cd^{2+}, Pb^{2+} and Hg^{2+} ions using aminosepiolite coated glassy carbon electrode: optimization of detection parameters via response surface methodology. J Anal Testing 3:295–305. https://doi.org/10.1007/s41664-019-00086-z
23. Jiokeng ZSL, Dongmo ML, Ymele E, Ngameni E, Tonle IK (2017) Sensitive stripping voltammetry detection of Pb(II) at a glassy carbon electrode modified with an amino-functionalized attapulgite. Sensors Actuators B Chem 242:1027–1034. https://doi.org/10.1016/j.snb.2016.09.150
24. Tonle KI, Ngameni E, Walcarius A (2005) Preconcentration and voltammetric analysis of mercury(II) at a carbon paste electrode modified with natural smectite-type clays grafted with organic chelating groups. Sensors Actuators B Chem 110:195–203. https://doi.org/10.1016/j.snb.2005.01.027
25. Ngassa PGB, Tonle IK, Walcarius A, Ngameni E (2014) One-step co-intercalation of cetyltrimethylammonium and thiourea in smectite and application of the organoclay to the sensitive electrochemical detection of Pb(II). Appl Clay Sci 99:297–305. https://doi.org/10.1016/j.clay.2014.07.014
26. Jiokeng ZSL, Tonle IK, Walcarius A (2019) Amino-attapulgite/mesoporous silica composite films generated by electro-assisted self-assembly for the voltammetric determination of diclofenac. Sensors Actuators B Chem 287:296–305. https://doi.org/10.1016/j.snb.2019.02.038
27. Tcheumi HL, Tassontio NV, Tonle IK, Ngameni E (2019) Surface functionalization of smectite-type clay by facile polymerization of ß-cyclodextrin using citric acid cross-linker: application as sensing material for the electrochemical determination of paraquat. Appl Clay Sci 173:97–106. https://doi.org/10.1016/j.clay.2019.03.013
28. Tchieno MMF, Guenang SL, Ymele E, Ngameni E, Tonle IK (2017) Electroanalytical application of amine-grafted attapulgite to the sensitive quantification of the bioactive compound mangiferin. Electroanalysis 29(2):529–537. https://doi.org/10.1002/elan.201600381
29. Ngassa PGB, Tonle KI, Ngameni E (2016) Square wave voltammetric detection by direct electroreduction of paranitrophenol (PNP) using an organosmectite film-modified

glassy carbon electrode. Talanta 147:547–555. https://doi.org/10.1016/j.talanta.2015.10.030
30. Chipera SJ, Bish DL (2001) Baseline studies of the clay minerals society source clays: powder X-ray diffraction analyses. Clay Clay Miner 49:398–409. https://doi.org/10.1346/CCMN.2001.0490507
31. Dongmo ML, Jiokeng ZSL, Pecheu NC, Walcarius A, Tonle IK (2020) Amino-grafting of montmorillonite improved by acid activation and application to the electroanalysis of catechol. Appl Clay Sci 191:105602. https://doi.org/10.1016/j.clay.2020.105602
32. Zhu BY, Murali S, Cai W, Li X, Suk JW, Potts JR, Ruoff RS (2010) Graphene and graphene oxide: synthesis, properties and applications. Adv Mater 22:3906–3924. https://doi.org/10.1002/adma.201001068
33. Casiraghi C, Hartschuh A, Qian H, Piscanec S, Georgi C, Fasoli A, Novoselav KS, Basko DM, Ferrari AC (2009) Raman spectroscopy of graphene edges. Nanoletter 9(4):1433–1441. https://doi.org/10.1021/nl8032697
34. Li J, Ye F, Vaziri S, Muhammed M, Lemme MC, Ostling M (2012) A simple route towards high-concentration surfactant-free graphene dispersions. Carbon 50(8):3092–3116. https://doi.org/10.1016/j.carbon.2012.03.011
35. Katti KS, Sikdar D, Katti DR, Ghosh P, Verma D (2006) Molecular interactions in intercalated organically modified clay and clay-polycaprolactam nanocomposites: experiments and modeling. Polymer 47(1):403–414. https://doi.org/10.1016/j.polymer.2005.11.055
36. Amarasinghe PM, Katti KS, Katti DR (2008) Molecular hydraulic properties of montmorillonite: a polarized Fourier transformed infrared spectroscopic study. Appl Spectrosc 62(12):1303–1313 https://www.osapublishing.org/as/abstract.cfmURI=as-62-12-1303
37. Mendelovici E (1973) Infrared study of attapulgite and HC1 treated attapulgite. Clay Clay Miner 21:115–119. https://doi.org/10.1346/CCMN.1973.0210207
38. Xue A, Zhou S, Zhao Y, Lu X, Han P (2011) Effective NH_2-grafting on attapulgite surfaces for adsorption of reactive dyes. J Hazard Mater 194:7–14. https://doi.org/10.1016/j.jhazmat.2011.06.018
39. Shanmugharaj AM, Rhee KY, Ryu SH (2006) Influence of dispersing medium on grafting of aminopropyltriethoxysilane in swelling clay materials. J Colloid Interface Sci 298:854–859. https://doi.org/10.1016/j.jcis.2005.12.049
40. Shen W, He H, Zhu J, Yuan P, Frost RL (2007) Grafting of montmorillonite with different functional silanes via two different reaction systems. J Colloid Interface Sci 313:268–273. https://doi.org/10.1016/j.jcis.2007.04.029
41. Shen W, He H, Zhu J, Yuan P, Ma Y, Liang X (2009) Preparation and characterization or 3-aminopropyltriethosysilane grafted montmorillonite and acid-activated montmorillonite. Chin Sci Bull 54:265–271. https://doi.org/10.1007/s11434-008-0361-y
42. Daniel LM, Frost RL, Zhu HY (2008) Edge-modification of laponite with dimethyloctylmethoxysilane. J Colloid Interface Sci 321:302–309. https://doi.org/10.1016/j.jcis.2008.01.032
43. He HP, Duchet J, Galy J, Gerard J (2005) Grafting of swelling clay materials with 3- aminopropyltriethoxysilane. J Colloid Interface Sci 288:171–176. https://doi.org/10.1016/j.jcis.2005.02.092
44. Su LN, Qi T, Hongping H, Jianxi Z, Peng Y (2012) Locking effect: a novel insight in the silylation of montmorillonite surfaces. Mater Chem Phys 136(2–3):292–295. https://doi.org/10.1016/j.matchemphys.2012.07.010
45. Celis R, Hermosin MC, Cornejo J (2000) Heavy metal adsorption by functionalized clays. Environ Sci Technol 34(21):4593–4599. https://doi.org/10.1021/es000013c
46. Tonle KI, Ngameni E, Njopwouo D, Carteret C, Walcarius A (2003) Functionalization of natural smectite-type clays by grafting with organosilanes: physico-chemical characterization and application to mercury(II) uptake. Phys Chem Chem Phys 5:4951–4961. https://doi.org/10.1039/B308787E
47. Mercier L, Pinnavaia TJ (1998) Heavy metal ion adsorbents formed by the grafting of a thiol functionality to mesoporous silica molecular sieves: factors affecting Hg(II) uptake. Environ Sci Technol 32:2749–2754. https://doi.org/10.1021/es970622t
48. Walcarius A, Delacote C (2003) Rates of access to the binding sites in organically modified silicates. 3. Effect of structure and density of functional groups in mesoporous solids obtained by the cocondensation route. Chem Mater 15:4181–4192. https://doi.org/10.1021/cm031089l
49. Tonle IK, Ngameni E, Walcarius A (2004) From clay to organoclay film modified electrodes: tuning charge selectivity in ion exchange voltammetry. Electrochim Acta 49:3435–3443. https://doi.org/10.1016/j.electacta.2004.03.012
50. Shih Y, Zen JM, Kumar AS, Chen PY (2004) Flow injection analysis of zinc pyrithione in hair care products on a cobalt phthalocyanine modified screen-printed carbon electrode. Talanta 62(5):912–917. https://doi.org/10.1016/j.talanta.2003.10.039
51. Laviron E (1979) General expression of the linear potential sweep voltammogram in the case of diffusionless electrochemical systems. J Electroanal Chem 101:19–28. https://doi.org/10.1016/S0022-0728(79)80075-3
52. Ghoneim MM, Hassanein AM, Hammam E, Beltagi AM (2000) Simultaneous determination of Cd, Pb, Cu, Sb, Bi, Se, Zn, Mn, Ni, Co and Fe in water by differential pulse stripping voltammetry at a hanging mercury drop electrode. Fres nius J Anal Chem 367:378–383. https://doi.org/10.1007/s002160000410
53. Stoj A, Szwajgier D, Baranowska-Wojcik E, Domagała D (2019) Gentisic acid, salicylic acid, total phenolic content and cholinesterase inhibitory activities of red wines made from various grape varieties. S Afr J Enol Vitic 40(1). https://doi.org/10.21548/40-1-2885
54. van Lelyveld LJ, van Vuuren SP, Visser G (1988) Gentisic acid concentration in healthy and greening infected fruit albedo and leaves of citrus species and cultivars. S Afr J Plant Soil 5(4):209–211. https://doi.org/10.1080/02571862.1988.10634987
55. Wendy RR, Aurelie L, Lorraine S, Gary JD, Garry GD (2009) Phenolic acid content of fruits commonly consumed and locally produced in Scotland. Food Chem 115:100–104. https://doi.org/10.1016/j.foodchem.2008.11.086
56. George JS, Eleftherios PD, Alex K, David MG (1997) A multiresidue derivatization gas chromatographic assay for fifteen phenolic constituents with mass selective detection. Anal Chem 69:4405–4409. https://doi.org/10.1021/ac961320x
57. Pirker R, Huck CW, Popp M, Bonn GK (2004) Simultaneous determination of gentisic, salicyluric and salicylic acid in human plasma using solid-phase extraction, liquid chromatography and electrospray ionization mass spectrometry. J Chromatogr B 809:257–264. https://doi.org/10.1016/j.jchromb.2004.06.031
58. Li W, Matthew SH, Douglas HS (2013) Simultaneous determination of gallic acid and gentisic acid in organic anion transporter expressing cells by liquid chromatography–tandem mass spectrometry. J Chromatogr B 937:91–96. https://doi.org/10.1016/j.jchromb.2013.08.024

.